

## MODELLING UNCERTAINTY IN AN UNDERWATER ACOUSTIC POSITIONING SYSTEM

Dugald Thomson<sup>1</sup>, Stan E. Dosso<sup>1</sup>, Emmett Gamroth<sup>2</sup> and Colin Bradley<sup>2</sup>

<sup>1</sup>School of Earth & Ocean Sciences and <sup>2</sup>Department of Mechanical Engineering  
University of Victoria, Victoria, BC, Canada, V8P 5C2, dugald@uvic.ca

### ABSTRACT

This paper develops a ray-based travel-time inversion to simulate the accuracy of an active underwater acoustic localization system, and examines the localization accuracy as a function of various sources of error and geometric and environmental factors. The system considered here simulates localizing an autonomous underwater vehicle using arrival times of acoustic transmissions from an onboard source as measured at hydrophones distributed spatially over a test range. Since localization uncertainty is a function of source location, uncertainties are calculated for the source at a grid of locations over the areas of the test bed. Localization accuracy is considered as a function of timing errors, uncertainty in hydrophone locations, target depth, variations in sound-speed profile, and hydrophone geometry.

### SOMMAIRE

Cet article développe un inversion de temps d'arrivée en traçant des rayons pour simuler la précision d'un système actif de localisation acoustiques sous-marins, et examine la précision de localisation en fonction de diverses sources d'erreur et de facteurs géométriques et environnementale. Le système considéré ici simule la localisation d'un véhicule autonome sous-marin en utilisant les instants d'arrivées des transmissions acoustiques provenant d'une source à bord tel que mesuré à partir d'hydrophones répartis spatialement sur une plage de test. Puisque l'incertitude de localisation est fonction de l'emplacement de la source, les incertitudes sont calculées pour la source à une grille de lieux sur les zones du banc d'essai. La précision de localisation est considérée comme une fonction de synchronisation des erreurs, l'incertitude dans l'emplacement des hydrophones, la profondeur des cibles, les variations du profile vitesse-son, et la géométrie des hydrophones.

## 1. INTRODUCTION

Precise positioning of autonomous underwater vehicles (AUVs) is an important problem for the ocean science community as it attempts to extend its reach further into the deeps. Terrestrial Global Positioning Systems (GPS) are of little use for an underwater target as the high-frequency/low-power signals they employ are unable to penetrate beyond the surface layers of the ocean due to reflection and absorption by the seawater. The Integrated Acoustic System (IAS) being designed by the University of Victoria's Ocean Technology Test Bed (OTTB) team aims to overcome this obstacle by developing a high-precision underwater acoustic positioning system. The goal is to produce a system, similar to a commercial Long Baseline unit, capable of positioning a target within the OTTB range to a sufficient accuracy for use as a ground truth for testing onboard navigation systems.

The range itself covers an area of approximately 1.5 km by 1.5 km, with five hydrophones moored to 3-m towers on the seabed at depths of 60 m to 130 m and located in the four corners of the range plus one near the centre, as depicted in Fig. 1. The N-S axis is referred to as  $y$  while the E-W axis is aligned to  $x$ , with  $z$  being depth below surface. The AUV will be outfitted with a generic 'pinger', a transducer that periodically emits an acoustic pulse in the 5-

80 kHz frequency range as it moves about the range. The pulse travels through the underwater medium, and is received at the five hydrophones stations (Gamroth, Kennedy & Bradley, 2011).

The received ping arrival instants represent the data, which are used to estimate the source position using the time difference of arrival through a ray-based linearized inversion technique. The error in the source position estimate is a function of clock error in the Precision Time Protocol (PTP) system ( $\pm 10 \mu\text{s}$ ), tower position survey error ( $\pm 0.40$  m in each of three dimensions expected), and errors in the measured sound-speed profile (due to instrument bias). Positional uncertainty is also affected to a large degree by the source/hydrophone geometry.

The sound-speed profiles used in this investigation are shown in Fig. 2. The solid-line profile was obtained from direct sound-speed measurements using a velocimeter cast at the range in Saanich Inlet, on November 8, 2011, a day with calm winds. The dashed-line profile was derived from temperature and salinity data collected by Zaikova et al. (2010) within Saanich Inlet but outside the OTTB range during February, 2008. Once the range is operational, the protocol will call for collection of a sound-speed profile within a few hours of data collection for use in target positioning.

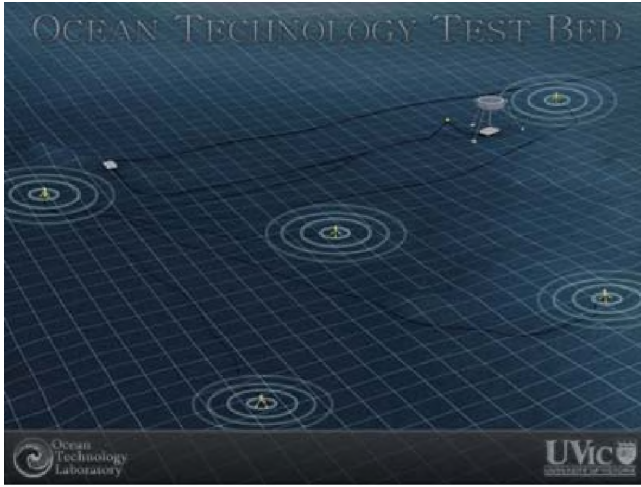


**Figure 1: Conceptual image of the OTTB range located in Saanich Inlet, near Victoria, BC, showing the five hydrophone tower locations and a grid representing the simulated target positions (Ocean Technology Test Bed, 2005).**

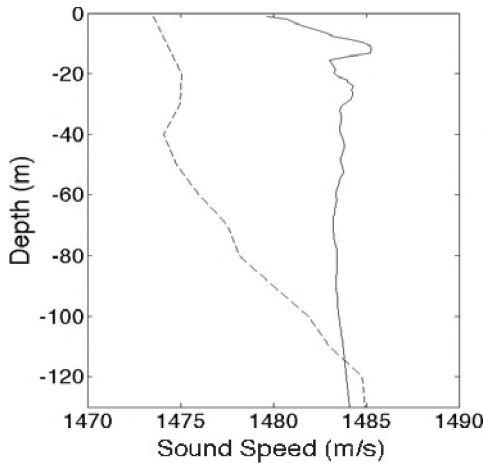


**Figure 2: Sound-speed profiles used in the simulations. The solid-line profile was collected during November, 2011. The dashed-line profile was collected by Hallam & Tortell (2008) during February, 2008.**

To examine the anticipated localization accuracy of the system, a simulation procedure was developed which calculates uncertainties for a series of positions about the range. The remainder of this paper describes the inversion algorithm used to compute localization uncertainties (Section 2) and gives a series of examples considering a variety of factors that affect the accuracy (Section 3).

## 2. METHOD

The modelling study carried out here to estimate the localization accuracy for a target located within the range is based on estimating the posterior uncertainties of the source-location in  $x$ ,  $y$ , and  $z$ . Since the source-location uncertainty varies with source location, uncertainties are calculated for the source at each point within a grid of positions over the area of the test bed. At each grid point, the source-location

uncertainties are estimated using a linearized Bayesian approach that includes the effects of arrival-time errors as well as uncertainties in hydrophone locations and sound speed. A complete description of these methods can be found in Dosso & Ebbeson (2006). The lateral ( $r$ ) uncertainty is calculated as the square root of the  $L_2$  norm of the horizontal ( $x$  and  $y$ ) uncertainty components.

The OTTB range is modelled as a range-independent, layered ocean using a measured sound-speed profile. The data set  $\mathbf{t}$  is the vector of  $N = H$  measured ray arrival times at the  $H = 5$  hydrophone stations, while the model  $\mathbf{m}$  is a vector of  $M = 3H + 5$  parameters representing source locations ( $x, y, z$ ), hydrophone positions ( $X_i, Y_i, Z_i$   $i = 1, \dots, 5$ ), source instant ( $t_0$ ), and an unknown constant bias to the sound-speed profile ( $\Delta c$ ) as

$$\mathbf{m} = \begin{bmatrix} x, y, z, \bar{c}t_0, X_1, Y_1, Z_1, \dots, X_i, Y_i, Z_i, \Delta c \\ \text{for } i = 1:H \end{bmatrix}^T \quad (1)$$

where the source instant  $t_0$  is multiplied by  $\bar{c}$ , a representative sound speed, to provide the same units and scale as positional parameters.

The observed data  $\mathbf{t}$  are the arrival times of pings originating from the target and received at the five hydrophone stations for each given source transmission. These data contain noise (errors) as discussed in Section 1, and the direct path ray arrival times  $\mathbf{t}$  can be written in general vector form as

$$\mathbf{t} = \mathbf{t}(\mathbf{m}) + \mathbf{n}, \quad (2)$$

where  $\mathbf{t}(\mathbf{m})$  are the predicted data based on the model parameters  $\mathbf{m}$ , i.e., the calculated travel times along eigenrays connecting source and receivers, and  $\mathbf{n}$  are errors on the data. The error  $n_i$  on datum  $t_i$  is assumed to be an independent Gaussian-distributed random process with zero mean and standard deviation  $\sigma$ .

Expanding  $\mathbf{t}(\mathbf{m})$  in a Taylor series to first order about an arbitrary starting model  $\mathbf{m}_0$ , the result can be written

$$\mathbf{d} = \mathbf{J}\mathbf{m}, \quad (3)$$

where

$$\mathbf{d} = \mathbf{t}(\mathbf{m}) - \mathbf{t}(\mathbf{m}_0) + \mathbf{J}\mathbf{m}_0 \quad (4)$$

are modified data and  $\mathbf{J}$  is the Jacobian matrix of partial derivatives of the data functionals with respect to the model parameters evaluated at  $\mathbf{m}_0$ :

$$J_{ij} = \partial d_i(\mathbf{m}_0) / \partial m_j. \quad (5)$$

This matrix is sometimes called the sensitivity matrix as it quantifies the sensitivity of the data to the model, and contains the physics and geometry of the forward problem.

Prior information about the model parameters is also considered in the problem. Assuming this prior information represents a Gaussian uncertainty distribution with expected values  $\hat{m}_k$  (the prior estimate for the  $k$ th parameter) and standard deviations  $\xi_k$ , the maximum *a posteriori* (MAP) solution is given by

$$\mathbf{m}_{\text{MAP}} = \hat{\mathbf{m}} + [\mathbf{J}^T \mathbf{C}_d^{-1} \mathbf{J} + \mathbf{C}_p^{-1}]^{-1} \mathbf{J}^T \mathbf{C}_d^{-1} (\mathbf{d} - \mathbf{J} \hat{\mathbf{m}}), \quad (6)$$

where  $\mathbf{C}_d = \sigma^2 \mathbf{I}$  is the data covariance matrix and  $\mathbf{C}_p = \text{diag}\{\xi_k^2\}$  is the prior model covariance matrix. Further, the posterior probability density is a Gaussian distribution about  $\mathbf{m}_{\text{MAP}}$  with posterior model covariance matrix

$$\mathbf{C}_m = [\mathbf{J}^T \mathbf{C}_d^{-1} \mathbf{J} + \mathbf{C}_p^{-1}]^{-1}. \quad (7)$$

The square root of the diagonal elements of  $\mathbf{C}_m$  provide posterior standard deviation (uncertainty) estimates for the model parameters.

Equation (7) represents a linearized approximation in this problem; however, comparison to non-linear solutions from Monte Carlo analysis (Dosso & Sotirin, 1999) indicates that linearization errors are small if  $\mathbf{m}_0$  is close to the true model. When inverting measured data this is usually realized by iterating the linearized solution to convergence.

The inversion techniques described above are based on a fast ray-tracing algorithm that uses Newton's method to determine eigenrays; analytic expressions for the ray derivatives are available for the Jacobian matrix (Dosso & Ebbeson, 2006).

In this paper, uncertainties in  $x$ ,  $y$ ,  $z$ , and  $r = \sqrt{x^2 + y^2}$  are taken from Eq. (7) and used to quantify the expected localization accuracy.

### 3. RESULTS

A series of simulations are presented here to compare the effects on localization accuracy of several factors: hydrophone positioning and sound-speed uncertainty, different source depths, and the effect of reducing target vertical positioning uncertainty through the addition of a depth sensor. The results of increased and decreased timing errors are also considered, as well as different sound-speed profiles and hydrophone geometric configurations.

The first simulation considers what is referred here to as the 'ideal-case' scenario, where the hydrophone positional uncertainty and the sound-speed profile bias are both assumed to be zero, with the timing uncertainty set to the PTP limit of 10  $\mu\text{s}$ . The source depth is 10 m, and the sound-speed profile is the solid line from Fig. 2 (common to all simulations unless otherwise noted). This represents the simplest case where only the uncertainty due to the system timing error is considered. The results of this simulation are shown in Fig. 3 in terms of  $x$ ,  $y$ ,  $r$ , and  $z$  uncertainties (colour contours) over the area of the range.

The effects of source/hydrophone geometry are immediately visible in Fig. 3. The smallest uncertainty in  $x$  is found for a source located between two or more hydrophones in  $x$ ; similarly, the lowest uncertainty in  $y$  occurs for a source between two or more hydrophones in  $y$ . The most accurate vertical positioning tends to occur for the source locations nearest a hydrophone, where the acoustic ray travels nearly vertically. The greatest horizontal uncertainty occurs for a source in the corners of the range, where the

source/hydrophone geometry is poor; the greatest vertical uncertainty tends to occur for a source furthest from a hydrophone, because the greatest amount of vertical information is contained in rays that arrive at steep vertical angles at the hydrophone.

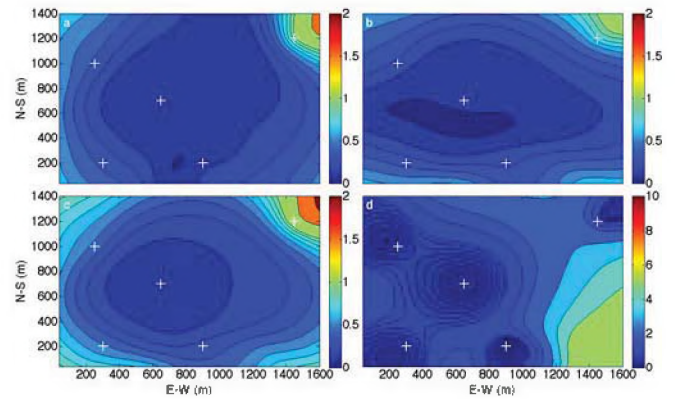


**Figure 3: Localization uncertainties for the 'ideal case' of perfectly known hydrophone locations and sound-speed profile. Panels (a)-(d) show absolute errors in  $x$ ,  $y$ ,  $r$ , and  $z$ , respectively, for a source at 10-m depth. contours represent uncertainty in metres. Hydrophone locations are depicted as white crosses.**

In the second example, the uncertainty from the 'standard case' is examined, where the timing uncertainties remain at 10  $\mu\text{s}$ , the hydrophones have positional uncertainties of 0.40 m in  $x$ ,  $y$ , and  $z$ , and the sound-speed profile has an uncertainty (bias) of 1 m/s. The target depth is again set to 10 m. The results of the simulation are shown in Fig. 4. The uncertainties are much greater than in the 'ideal case', indicating that relatively small uncertainties in hydrophone location and sound-speed profile can have a significant effect on AUV localization accuracy and must be taken into account in a meaningful modelling study.

The smallest uncertainties for the  $x$  component in Fig. 4(a) are found in the middle of the range and aligned N-S, as these locations produce the most favourable hydrophone geometry for estimating the position in  $x$ , due to the rays arriving with large  $x$  components. Similarly for the  $y$  component, in Fig. 4(b), the smallest uncertainties also tend to the centre but the alignment is E-W. Additionally, the horizontal uncertainty components tend to be lower in the southern and western regions of the range, as the northeastern hydrophone is asymmetrically located at a longer interval than the typical spacing between other hydrophones. This greater span increases the region of poor geometry within the range, whereas in the south and west regions, a higher proportion of the area produces favourable geometric alignments in  $x$  and  $y$ .

Figure 4(c) shows the uncertainty in  $r$ , which combines the uncertainty of  $x$  and  $y$ . The region of small uncertainty has a rounded symmetrical shape as opposed to the linear shape in the individual  $x$  and  $y$  components, and the combined uncertainty is always greater than either constituent component. The vertical uncertainty in Fig. 4(d) is lowest for a target located close to any hydrophone, with



increasing uncertainty for targets that are further away from a hydrophone.

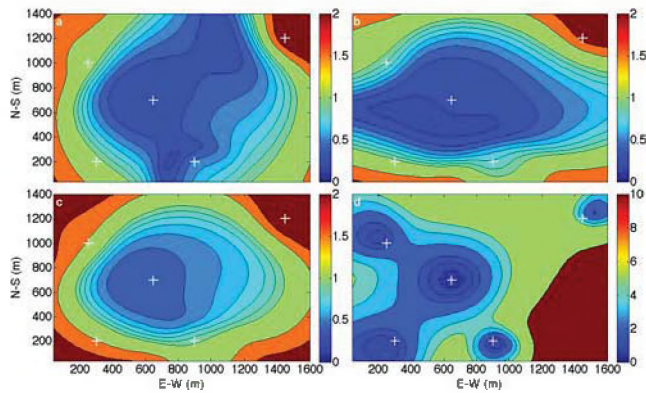


**Figure 4: Localization uncertainties for the ‘standard-case’ scenario. Panels (a)-(d) show absolute errors in  $x$ ,  $y$ ,  $r$ , and  $z$ , respectively, for a source at 10-m depth. Colour contours represent uncertainty in metres. Hydrophone locations are depicted as white crosses.**

The effect of varying target depth is presented in Fig. 5, which shows the result for the same simulation parameters but with a target at 40-m depth. The horizontal results are similar to the 10-m depth case shown in Fig. 4; however, the geometric effects are more pronounced with the deeper target, due to the reduced vertical extent between source and receiver. In  $z$ , the uncertainty increases for the deeper target especially in areas of the range distant from a hydrophone, where uncertainty is relatively high. This scenario was repeated for multiple source depths (not shown). For targets at greater depths, the vertical uncertainty increases, since the ray arrives at the hydrophone more horizontally, providing less vertical information about the target position. Hence, the IAS system is ineffective at estimating the depth of a deep source.

In investigating ways to overcome this limitation and to improve overall uncertainty, a scenario was simulated where the target is outfitted with a depth sensor, so that its vertical positioning is always known to within 0.03 m, shown in Fig 6. In this simulation the posterior uncertainty in  $z$  is  $\leq 0.03$  m throughout the range. The effect of this improved uncertainty on the lateral uncertainty varies depending on the location within the range. For the locations with relatively low uncertainty (those with the most favourable geometry), the uncertainty is improved only slightly, typically on the order of 2%. However, in the regions where uncertainty is high, as well as locations near a hydrophone, the improvement is much more significant: as much as 70%.

To consider next the effect of timing errors, a simulation was run where the timing uncertainty was increased by a factor of 100 to 1 ms. The results are presented in Fig. 7, and show that uncertainty is substantially increased for all components, indicating that timing uncertainty is an important contributor to overall target positional uncertainty. The 1 ms error was chosen because this is a representative timing accuracy in a typical system employing Network Timing Protocol, as opposed to the

10  $\mu$ s accuracy achieved in a PTP network (Lentz & Lecroart, 2009). This finding indicates that a high-precision acoustic positioning system would not be feasible without a PTP network.

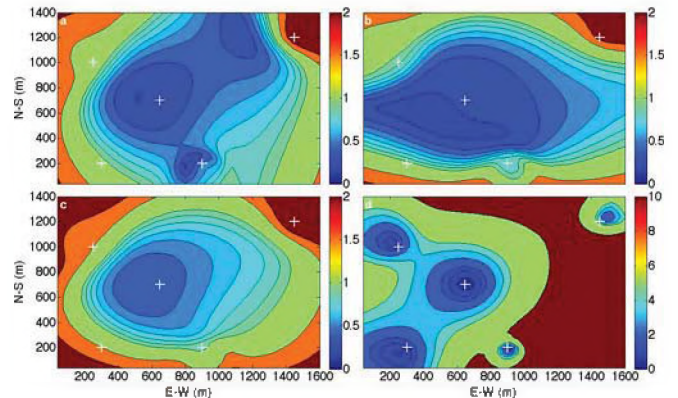


**Figure 5: Localization uncertainties for the ‘standard-case’ scenario. Panels (a)-(d) show absolute errors in  $x$ ,  $y$ ,  $r$ , and  $z$ , respectively, for a source at 40-m depth. Colour contours represent uncertainty in metres. Hydrophone locations are depicted as white crosses.**

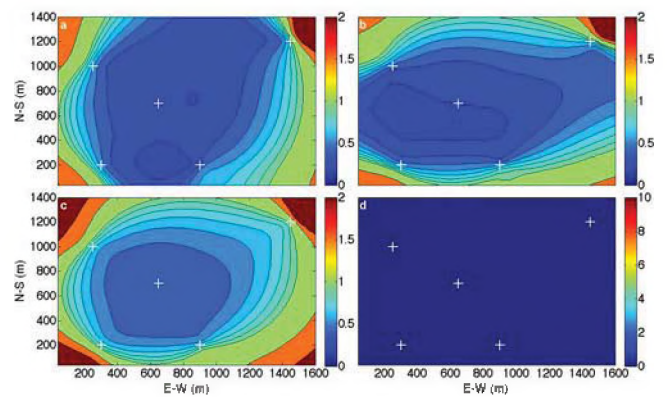


**Figure 6: Localization uncertainties for the ‘depth-sensor case’ scenario with target position in  $z$  assumed to be known to within 0.03 m uncertainty due to a depth sensor. Panels (a)-(d) show absolute errors in  $x$ ,  $y$ ,  $r$ , and  $z$ , respectively, for a source at 10-m depth. Colour contours represent uncertainty in metres. Hydrophone locations are depicted as white crosses.**

Another aspect of the PTP network is the potential to further increase the timing precision; it is anticipated that further development in network timing protocols will allow for timing precision to within 100s of nanoseconds (Lentz & Lecroart, 2009). These improvements could be incorporated into the IAS in the future, so a simulation was carried out reducing timing uncertainty by a factor of 100 to 100 ns, shown in Fig. 8. The results are virtually identical to the ‘standard case’ (Fig. 4) with timing uncertainty 100 times greater, indicating that there exists a limit, near the PTP timing uncertainty of 10  $\mu$ s, beyond which the overall positional uncertainty is not impacted by further improvement; rather, the uncertainty in hydrophone positions becomes the limiting factor.

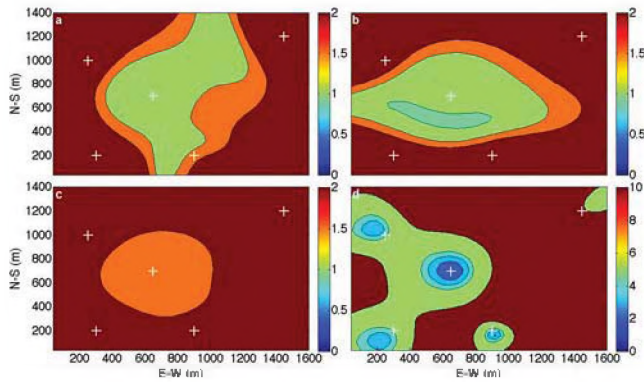


Figure 7: Localization uncertainties for the ‘standard-case’ scenario with a timing error of 1 ms. Panels (a)-(d) show absolute errors in  $x$ ,  $y$ ,  $r$ , and  $z$ , respectively, for a source at 10-m depth. Colour contours represent uncertainty in metres. Hydrophone locations are depicted as white crosses.

To determine whether the localization accuracy would be expected to vary significantly during the year as a function of seasonal variations to the sound-speed profile, Fig. 9 shows the ‘standard-case’ scenario run using the upward-refracting February profile shown in Fig. 2. The most notable difference from the standard-profile results (Fig. 4) is the increased uncertainty in the  $x$  and  $y$  components for target locations furthest from a hydrophone, and in  $z$  for target locations nearer a hydrophone. However, the variation in uncertainty due to sound-speed profile difference is generally small, indicating that the IAS should function consistently throughout the year.

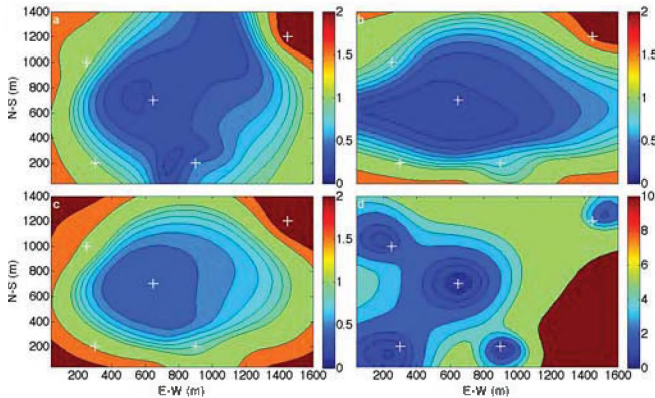


Figure 8: Localization uncertainties for the ‘standard-case’ scenario with a timing error of 100 ns. Panels (a)-(d) show absolute errors in  $x$ ,  $y$ ,  $r$ , and  $z$ , respectively, for a source at 10-m depth. Colour contours represent uncertainty in metres. Hydrophone locations are depicted as white crosses.

Finally, a simulation was carried out investigating the effects of moving the NE hydrophone tower in line with the other hydrophones to create a more symmetric range. The results are presented in Fig. 10, and show that by moving this hydrophone closer to the others, the uncertainty improves slightly for target locations contained within the

perimeter of hydrophones, but becomes substantially worse outside this perimeter.

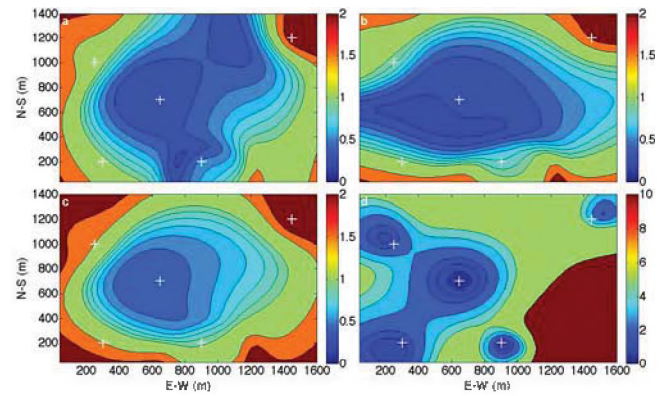


Figure 9: Localization uncertainties for the ‘standard-case’ scenario using a February sound-speed profile. Panels (a)-(d) show absolute errors in  $x$ ,  $y$ ,  $r$ , and  $z$ , respectively, for a source at 10-m depth. Colour contours represent uncertainty in metres. Hydrophone locations are depicted as white crosses.

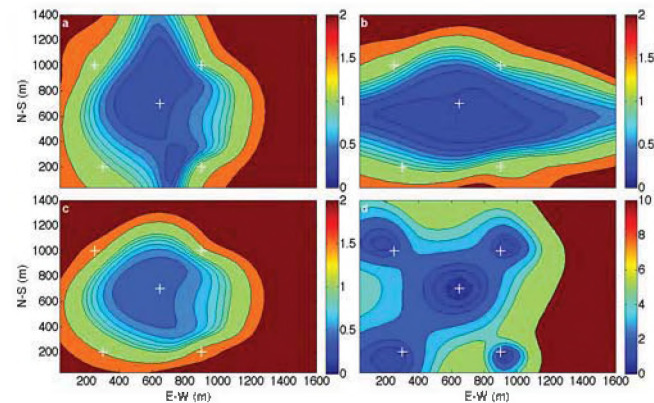


Figure 10: Localization uncertainties for the ‘standard-case’ scenario, relocating the NE hydrophone tower closer to the others. Panels (a)-(d) show absolute errors in  $x$ ,  $y$ ,  $r$ , and  $z$ , respectively, for a source at 10-m depth. Colour contours represent uncertainty in metres. Hydrophone locations are depicted as white crosses.

#### 4. DISCUSSION

This paper developed and illustrated a simulation procedure to investigate localization accuracy for an underwater target (AUV) in an acoustic test range. The simulation procedure allows examination of the effects of several factors, which are integral to the overall system performance, and is a valuable tool for predicting localization accuracy in a variety of situations. In this paper, localization uncertainty is examined as a function of hydrophone positional uncertainty, sound-speed uncertainty, timing errors, and source depth. The effect of reducing target positional uncertainty by employing an AUV-mounted depth sensor is also considered. Finally, different sound-speed



profiles and hydrophone geometric configurations are examined.

The simulation is especially beneficial for determining the expected baseline uncertainty for the range given specific values for the system factors (e.g. timing errors, hydrophone-positional and sound-speed uncertainties). In determining whether a certain static accuracy throughout the range is a realizable goal, localization uncertainties can be computed using realistic values for these system factors. Further, the effect of varying these factors on localization accuracies can be quantified.

It was shown that for the standard case (timing uncertainties of 0.1 ms, hydrophone location uncertainties of 0.4 m, sound-speed uncertainties of 1 m/s, 10 m source depth) the minimum positional uncertainty at any point in the range was on the order of 40 cm laterally, and 70 cm vertically. These smallest lateral uncertainties occur near the centre of the range, while the smallest vertical uncertainties are generally found above hydrophones. The largest uncertainties, extending well above 1 m, occur towards the periphery of the range due to less favourable source/hydrophone geometry.

Simulations show that for the existing range infrastructure, a high-precision acoustic positioning system is not feasible using standard network protocol due to the timing uncertainty. Using the PTP network timing, the timing accuracy is sufficient to allow high-precision positioning. However, the improvement in positional uncertainty from further development of the PTP timing uncertainty is negligible, indicating that the operational limit


has been met for timing error improvement and improvement in hydrophone localization would be required.

While the methods described here are applied to the specific case of the University of Victoria's OTTB, the approach is general and can be applied to model and examine the accuracy of any underwater acoustic positioning system.

## REFERENCES

- [1] Ocean Technology Test Bed (2005). *Integrated Acoustic System*. Retrieved January 24, 2011, from LACIR: Ocean Technology: <http://web.uvic.ca/~lacir/ocean/acoustics.php>.
- [2] Gamroth, E., Kennedy, J. & Bradley, C. (2011). Design and testing of an acoustic ranging technique applicable for an underwater positioning system. *Underwater Technology*, 29 (4), 183-193.
- [3] Zaikova, E., Walsh, D., Stilwell, C., Mohn, W., Tortell, P. & Hallam, S. (2010). Microbial community dynamics in a seasonally anoxic fjord: Saanich Inlet, British Columbia. *Environmental Microbiology*, 12 (1), 172-191.
- [4] Dosso, S.E. & Ebbeson, G. (2006). Array element localization accuracy and survey design. *Canadian Acoustics*, 34(4), 1-11.
- [5] Dosso, S.E. & Sotirin, B. (1999). Optimal array element localization. *Journal of the Acoustical Society of America*, 106, 3445-3459.
- [6] Lentz, S. & Lecroart, A. (2009). Precision timing in the NEPTUNE Canada network. *OCEANS 2009-EUROPE*, 1-5.

Discover new heights in acoustics design

 **Odeon** Room Acoustics Software

[www.odeon.dk](http://www.odeon.dk)